X-ray polarimetry of the accreting pulsar GX 301–2

Valery F. Suleimanov, Sofia V. Forsblom, Sergey S. Tsygankov, Juri Poutanen, Victor Doroshenko, Rosalia Doroshenko, Fiamma Capitanio, Alessandro Di Marco, Denis González-Caniulef, Jeremy Heyl, et al.

▶ **To cite this version:**

Valery F. Suleimanov, Sofia V. Forsblom, Sergey S. Tsygankov, Juri Poutanen, Victor Doroshenko, et al.. X-ray polarimetry of the accreting pulsar GX 301–2. Astronomy and Astrophysics - A&A, 2023, 678, 10.1051/0004-6361/202346994 . insu-04254810

HAL Id: insu-04254810

https://insu.hal.science/insu-04254810v1

Submitted on 26 Oct 2023

HAL is a multi-disciplinary open access archive for the deposit and dissemination of scientific research documents, whether they are published or not. The documents may come from teaching and research institutions in France or abroad, or from public or private research centers.

L'archive ouverte pluridisciplinaire **HAL**, est destinée au dépôt et à la diffusion de documents scientifiques de niveau recherche, publiés ou non, émanant des établissements d'enseignement et de recherche français ou étrangers, des laboratoires publics ou privés.

Distributed under a Creative Commons Attribution 4.0 International License

A&A 678, A119 (2023)
https://doi.org/10.1051/0004-6361/202346994
© The Authors 2023

Astronomy & Astrophysics

X-ray polarimetry of the accreting pulsar GX 301−2

Valery F. Suleimanov[1], Sofia V. Forsblom[2], Sergey S. Tsygankov[2], Juri Poutanen[2], Victor Doroshenko[1], Rosalia Doroshenko[1], Fiamma Capitanio[3], Alessandro Di Marco[3], Denis González-Caniulef[4], Jeremy Heyl[5], Fabio La Monaca[3], Alexander A. Lutovinov[6], Sergey V. Molkov[6], Christian Malacaria[7], Alexander A. Mushtukov[8], Andrey E. Shtykovsky[6,9], Iván Agudo[10], Lucio A. Antonelli[11,12], Matteo Bachetti[13], Luca Baldini[14,15], Wayne H. Baumgartner[16], Ronaldo Bellazzini[14], Stefano Bianchi[17], Stephen D. Bongiorno[16], Raffaella Bonino[18,19], Alessandro Brez[14], Niccolò Bucciantini[20,21,22], Simone Castellano[14], Elisabetta Cavazzuti[23], Chien-Ting Chen[24], Stefano Ciprini[25,12], Enrico Costa[3], Alessandra De Rosa[3], Ettore Del Monte[3], Laura Di Gesu[23], Niccolò Di Lalla[26], Immacolata Donnarumma[23], Michal Dovčiak[28], Steven R. Ehlert[16], Teruaki Enoto[29], Yuri Evangelista[3], Sergio Fabiani[3], Riccardo Ferrazzoli[3], Javier A. Garcia[30], Shuichi Gunji[31], Kiyoshi Hayashida[32,⋆], Wataru Iwakiri[33], Svetlana G. Jorstad[34,35], Philip Kaaret[16], Vladimir Karas[28], Fabian Kislat[36], Takao Kitaguchi[29], Jeffery J. Kolodziejczak[16], Henric Krawczynski[37], Luca Latronico[18], Ioannis Liodakis[38], Simone Maldera[18], Alberto Manfreda[39], Frédéric Marin[40], Andrea Marinucci[23], Alan P. Marscher[34], Herman L. Marshall[41], Francesco Massaro[18,19], Giorgio Matt[17], Ikuyuki Mitsuishi[42], Tsunefumi Mizuno[43], Fabio Muleri[3], Michela Negro[44,45,46], Chi-Yung Ng[47], Stephen L. O'Dell[16], Nicola Omodei[26], Chiara Oppedisano[18], Alessandro Papitto[11], George G. Pavlov[48], Abel L. Peirson[26], Matteo Perri[12,11], Melissa Pesce-Rollins[14], Pierre-Olivier Petrucci[27], Maura Pilia[13], Andrea Possenti[13], Simonetta Puccetti[12], Brian D. Ramsey[16], John Rankin[3], Ajay Ratheesh[3], Oliver J. Roberts[24], Roger W. Romani[26], Carmelo Sgrò[14], Patrick Slane[49], Paolo Soffitta[3], Gloria Spandre[14], Douglas A. Swartz[24], Toru Tamagawa[29], Fabrizio Tavecchio[50], Roberto Taverna[51], Yuzuru Tawara[42], Allyn F. Tennant[16], Nicholas E. Thomas[16], Francesco Tombesi[52,25,53], Alessio Trois[13], Roberto Turolla[51,54], Jacco Vink[55], Martin C. Weisskopf[16], Kinwah Wu[54], Fei Xie[56,3], and Silvia Zane[54]

(Affiliations can be found after the references)

Received 24 May 2023 / Accepted 3 August 2023

ABSTRACT

The phase- and energy-resolved polarization measurements of accreting X-ray pulsars (XRPs) allow us to test different theoretical models of their emission, and they also provide an avenue to determine the emission region geometry. We present the results of the observations of the XRP GX 301−2 performed with the Imaging X-ray Polarimetry Explorer (IXPE). A persistent XRP, GX 301−2 has one of the longest spin periods known: ∼680 s. A massive hyper-giant companion star Wray 977 supplies mass to the neutron star via powerful stellar winds. We did not detect significant polarization in the phase-averaged data when using spectro-polarimetric analysis, with the upper limit on the polarization degree (PD) of 2.3% (99% confidence level). Using the phase-resolved spectro-polarimetric analysis, we obtained a significant detection of polarization (above 99% confidence level) in two out of nine phase bins and a marginal detection in three bins, with a PD ranging between ∼3% and ∼10% and a polarization angle varying in a very wide range from ∼0° to ∼160°. Using the rotating vector model, we obtained constraints on the pulsar geometry using both phase-binned and unbinned analyses, finding excellent agreement. Finally, we discuss possible reasons for a low observed polarization in GX 301−2.

Key words. magnetic fields – methods: observational – polarization – stars: neutron – X-rays: binaries – X-rays: individuals: GX 301-2

1. Introduction

Accreting X-ray pulsars (XRPs; see Mushtukov & Tsygankov 2022, for a recent review) are highly magnetized neutron stars (NSs) with a surface magnetic field strength of 10^{12}–10^{13} G orbiting early-type (typically O-B) donor stars. A pulsar accretes matter lost by the donor star through the stellar wind or, in the case of Be systems, a decretion disk. In some systems, an accretion disk around the NS may also form. The accretion flow in the vicinity of the NS surface is governed by the magnetic field, and the accreting matter forms hotspots near the NS magnetic poles radiating in the X-ray band. There are no commonly accepted models of the radiating regions; however, it is clear that at high enough mass accretion rates, the emitting hotspots transform to radially extended accretion columns (Basko & Sunyaev 1976; Becker et al. 2012; Mushtukov et al. 2015).

Radiation generated by plasma in a strong magnetic field was previously expected to be highly polarized at the photon energies below the cyclotron energy because of the birefringence of magnetized plasma (see, e.g., Harding & Lai 2006; Caiazzo & Heyl 2021). Testing this prediction recently became possible thanks to the Imaging X-ray Polarimetry Explorer (IXPE), as it allows one to measure X-ray polarization in the 2–8 keV energy band. In the first year of its operation, IXPE has carried out polarization measurements of several XRPs (Her X-1, Doroshenko et al. 2022; Cen X-3,

⋆ Deceased.

Open Access article, published by EDP Sciences, under the terms of the Creative Commons Attribution License (https://creativecommons.org/licenses/by/4.0), which permits unrestricted use, distribution, and reproduction in any medium, provided the original work is properly cited.
This article is published in open access under the Subscribe to Open model. Subscribe to A&A to support open access publication.

Tsygankov et al. 2022; 4U 1626−67, Marshall et al. 2022; Vela X-1, Forsblom et al. 2023; GRO J1008−57, Tsygankov et al. 2023; EXO 2030+375, Malacaria et al. 2023; X Persei, Mushtukov et al. 2023; LS V +44 17, Doroshenko et al. 2023). In most cases, the observations revealed a rather low pulse-phase averaged polarization degree (PD). The reason for the low PD is not completely clear. A toy model considering the upper layer of an NS atmosphere overheated by accretion has been proposed (Doroshenko et al. 2022). According to this model, the escaping radiation can be depolarized due to partial mode conversion when passing through the vacuum resonance region situated at the sharp temperature gradient between the cool inner atmospheric layers and the upper overheated layers. Additionally, variations of the polarization angle (PA) with the pulsar phase can lead to strong depolarization in the total signal.

The accreting XRP GX 301−2 (also associated with 4U 1223−62) is one of IXPE's targets. It is a high-mass X-ray binary system containing a slowly rotating ($P_{\rm spin} \sim 680$ s, White et al. 1976) NS orbiting the hyper-giant donor star Wray 977 (Hammerschlag-Hensberge et al. 1976). The donor star is very massive (39–53 $M_\odot$) and large ($\sim 62\,R_\odot$) with a huge mass-loss rate of $\dot{M} \sim 10^{-5}\,M_\odot\,{\rm yr}^{-1}$ via a dense and slow (∼300–400 km s^{-1}) wind (Kaper et al. 2006). The system inclination has been constrained to be in the range of 52°–78°, with an indication of a preference for an inclination closer to the lower end of the range (Leahy & Kostka 2008). A distance to the system of $3.53^{+0.40}_{-0.52}$ kpc was measured by *Gaia* (Treuz et al. 2018; Bailer-Jones et al. 2018). The orbital period of the system is known with a high accuracy: $P_{\rm orb} = 41.482 \pm 0.001$ d (Doroshenko et al. 2010). The NS orbit is elliptic with an eccentricity $e \sim 0.46$ (Koh et al. 1997), and the X-ray luminosity of the pulsar increases near the periastron, reaching $\sim 10^{37}$ erg s^{-1}(see Fig. 1 for the long-term light curve). The wind accretion picture in this system is very complicated. The outburst maximum is about 1.4 d before the periastron, and there is a secondary X-ray flux increase near the apoastron at the orbital phase 0.5 (Pravdo et al. 1995; Koh et al. 1997). It was even hypothesized that the NS in the system exhibits retrograde rotation (Mönkkönen et al. 2020).

The X-ray spectrum of the system has been investigated by many observatories, including *NuSTAR* (see Nabizadeh et al. 2019, and references therein). The continuum X-ray spectrum is typical for an accreting XRP and is well described by a power-law model with a Fermi-Dirac cutoff (Fürst et al. 2018) and some additional components. These include two cyclotron resonant scattering features near 35 and 50 keV (Fürst et al. 2018), whose energies are positively correlated with the source X-ray luminosity, including variations over the pulse period (Fürst et al. 2018; Nabizadeh et al. 2019). It is necessary to mention a strong local absorption that is also correlated with the observed luminosity. The absorber column density can be as high as $(5-20) \times 10^{23}$ cm^{-2} (see, e.g., Fürst et al. 2018; Nabizadeh et al. 2019; Doroshenko et al. 2010; Ji et al. 2021). Important components of the softer part of the X-ray spectrum are the iron Kα and Kβ lines, arising due to a reprocessing of X-rays in the matter surrounding the NS (see detailed analysis in Ji et al. 2021). Their strength is also strongly correlated with the source luminosity.

The first attempt to measure the X-ray polarization of GX 301−2 was performed with balloon-borne hard X-ray polarimeter X-Calibur in the 15–35 keV energy band. This attempt resulted in a non-detection (Abarr et al. 2020) due to a rather short flight duration.

In this work, we present the results of IXPE observations of GX 301−2. The IXPE observations were accompanied by simultaneous observations performed with the Spectrum Roentgen Gamma (SRG) observatory.

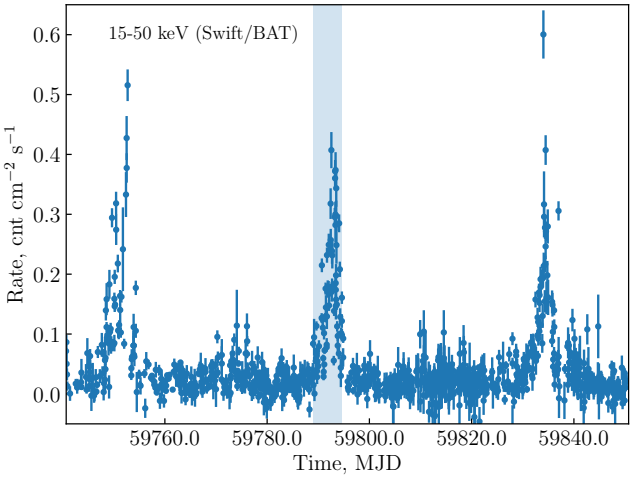

Fig. 1. Long-term light curve of GX 301−2 in the 15–50 keV energy band obtained with the *Swift*/BAT monitor. The shaded region represents the time of the IXPE observation.

2. Observations and data reduction

The IXPE observatory, a NASA mission in partnership with the Italian space agency (see a detailed description in Weisskopf et al. 2022), was launched by a Falcon 9 rocket on 2021 December 9. There are three grazing incidence telescopes onboard the observatory. Each telescope is composed of an X-ray mirror assembly and a polarization-sensitive detector unit (DU) equipped with a gas-pixel detector (Soffitta et al. 2021; Baldini et al. 2021). These instruments provide imaging polarimetry in the 2–8 keV energy band with a time resolution better than 10 µs.

Between 2022 July 29 and August 3, IXPE observed GX 301−2 with a total exposure of ≃290 ks per telescope. The data were processed with the IXPEOBSSIM package version 30.2.1 (Baldini et al. 2022) using the CalDB released on 2022 November 17. Before the scientific analysis, a position offset correction and energy calibration were applied. Source photons were collected in a circular region with a radius $R_{\rm src} = 70''$ centered at the GX 301−2 position. In the 2–8 keV band, the background makes up about 1.2% of the total count rate in the source region. Because of the low background level and the high source count rate, the background was not subtracted as recommended by Di Marco et al. (2023). The event arrival times were corrected to the Solar system barycenter using the standard `barycorr` tool from the FTOOLS package and accounting for the effects of binary motion using the orbital parameters from Doroshenko et al. (2010).

The polarimetric parameters of GX 301−2 were extracted utilizing the `pcube` algorithm (`xpbin` tool) in the IXPEOBSSIM package, which has been implemented following the formalism by Kislat et al. (2015). For the spectro-polarimetric analysis, the Stokes spectra I, Q, and U for the source region were prepared using the `xpbin` tool's `PHA1`, `PHA1Q`, and `PHA1U` algorithms in IXPEOBSSIM, resulting in a data set of nine spectra (three for each DU).

The flux (Stokes parameter I) energy spectra were binned to have at least 30 counts per energy channel. The same energy binning was also applied to the spectra of the Stokes parameters

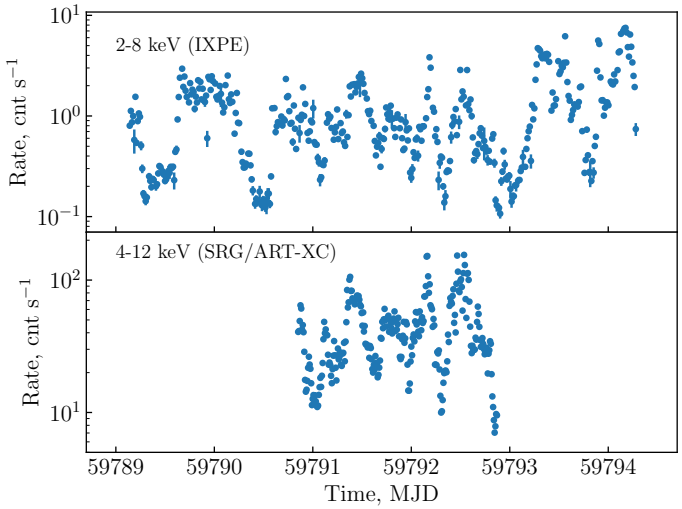

Fig. 2. Background subtracted light curve of the source in the 2–8 keV energy band observed with IXPE (top) and in the 4–12 keV band observed with SRG/ART-XC (bottom). Data from the three IXPE telescopes and the seven ART-XC telescopes were combined.

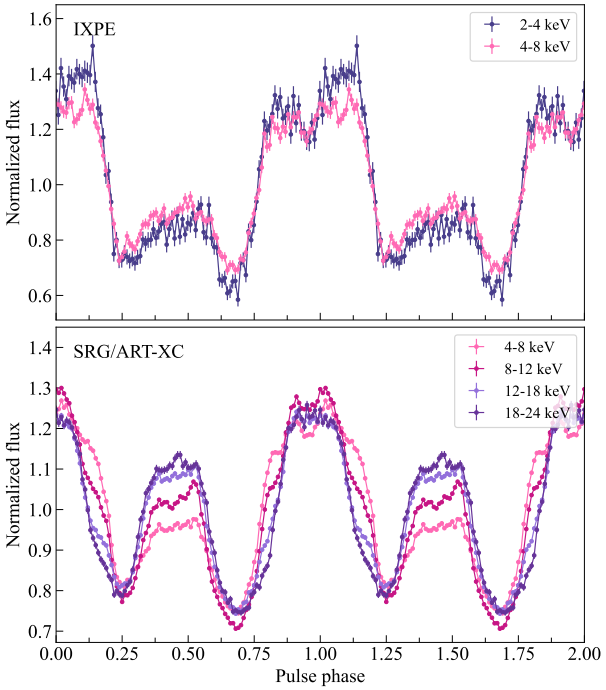

Fig. 3. Pulse profiles of GX 301−2 obtained by IXPE and ART-XC in different energy bands.

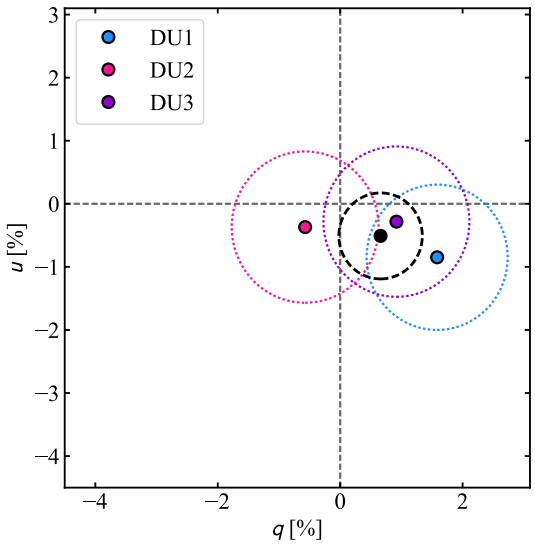

Fig. 4. Phase-averaged normalized Stokes parameters q and u for each DU and combining the DUs (in black) for the full 2–8 keV energy band. The circle size corresponds to the uncertainty at 68% confidence level.

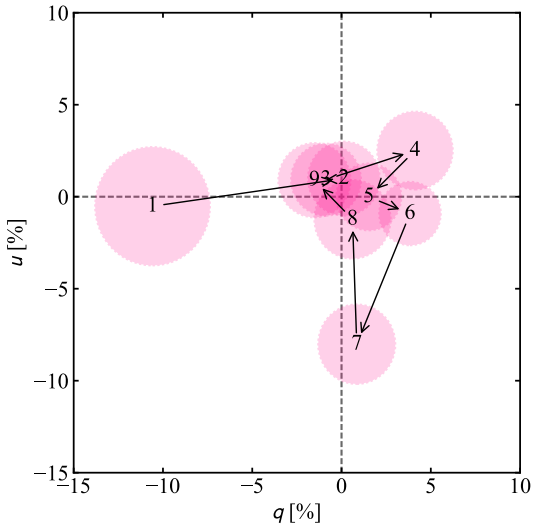

Fig. 5. Normalized Stokes parameters q and u for the phase-resolved polarimetric analysis using `pcube` (DUs combined) for the full 2–8 keV energy band. Each circle corresponds to a separate phase bin and is numbered according to its order as referenced in Table 1. The radius of the circle corresponds to a 1σ uncertainty.

Q and U. We applied the unweighted analysis (i.e., taking all events into account independently of the quality of the track reconstruction) of the IXPE data. All the spectra were fitted with the XSPEC package Arnaud (1996; version 12.12.1), which is a part of the standard high-energy astrophysics software suite `HEASOFT`, using the instrument response functions of version 12 and a χ^2 statistic. The uncertainties are given at the 68.3% confidence level unless stated otherwise.

The Mikhail Pavlinsky ART-XC telescope (Pavlinsky et al. 2021) on board the SRG observatory (Sunyaev et al. 2021) carried out simultaneous observations of GX 301−2 with IXPE starting on 2022 July 30 at 20:25 and ending on August 1 at 20:50 (UTC) with a total exposure of ∼160 ks. The ART-XC is a grazing incidence focusing X-ray telescope that provides imaging, timing, and spectroscopy in the 4–30 keV energy range. The telescope consists of seven identical modules and has a total effective area of ∼450 cm^2 at 8 keV, an angular resolution of 45″, an energy resolution of 1.4 keV at 6 keV, and a timing resolution of 23 µs. The ART-XC data were processed with the analysis software ARTPRODUCTS v1.0 with the CALDB version 20220908.

3. Results

3.1. Light curve and pulse profile

Between 2022 July 29 and August 3, GX 301−2 was observed during a pre-periastron flare (at the orbital phase approximately

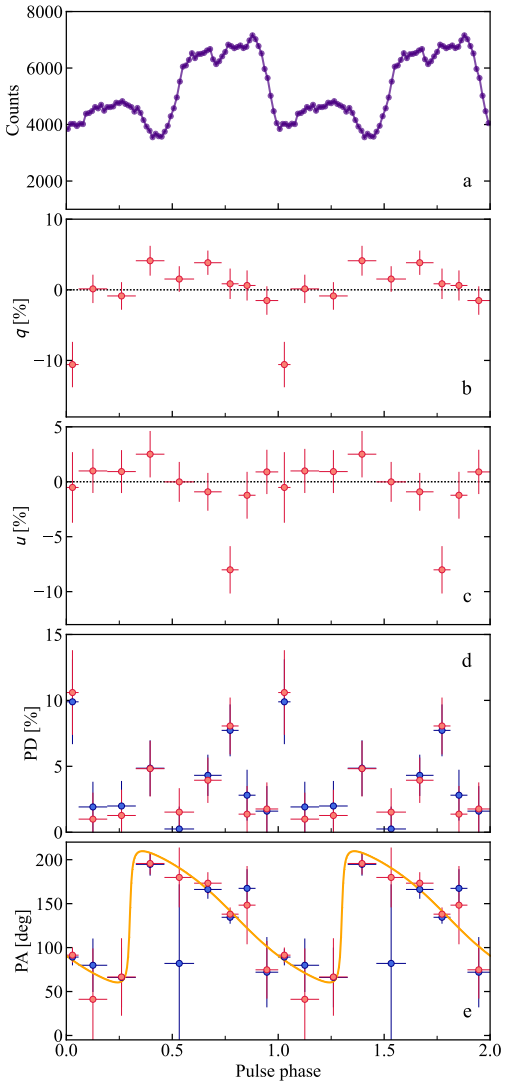

Fig. 6. Results from the pulse-phase-resolved analysis of GX 301−2 in the 2–8 keV range combining data from all DUs. *Panel a*: pulse profile. *Panels b* and *c*: dependence of the Stokes q and u parameters obtained from the pcube algorithm on the pulse phase. *Panels d* and *e*: PD and PA obtained with pcube and from the phase-resolved spectro-polarimetric analysis using XSPEC (shown by the red and blue symbols, respectively). The orange curve in *panel e* shows the best-fit RVM with $i_p = 135°$, $\theta = 43°$, $\chi_p = 135°$, and $\phi_0/(2\pi) = -0.2$ to the PAs obtained from the pairs of (q, u) (see Sect. 4.1).

0.95–1.00), as can be seen in the light curve shown in Fig. 1 and that was obtained by the *Swift*/BAT (Gehrels et al. 2004) monitor.[1] The light curves of GX 301−2 in the 2–8 energy band obtained with the IXPE observatory as well as with SRG/ART-XC in the 4–12 keV band are shown in Fig. 2. The spin period for GX 301−2 was measured from the IXPE data to be $P_{spin} = 670.644(2)$ s. The pulsed fraction in the 2–8 keV energy range of IXPE was determined to be $PF = 34.0\% \pm 1.1\%$, defined according to the equation $PF = (F_{max} - F_{min})/(F_{max} + F_{min})$, where F_{max} and F_{min} are the maximum and minimum count rates in the pulse profile, respectively. The pulse profiles of GX 301−2 as seen by IXPE and ART-XC in different energy bands are shown in Fig. 3. The phase-zero was chosen to coincide for the IXPE and ART-XC observations, and the phase-shift was determined

[1] https://swift.gsfc.nasa.gov/results/transients/

Table 1. Normalized q and u Stokes parameters and PD and PA in different phase bins obtained from the pcube algorithm.

Phase	q (%)	u (%)	PD (%)	PA (deg)
0.000–0.058	-10.6 ± 3.2	-0.5 ± 3.2	10.6 ± 3.2	-89 ± 9
0.058–0.193	0.1 ± 2.0	1.0 ± 2.0	$1.0^{+2.0}_{-1.0}$	41 ± 58
0.193–0.328	-0.9 ± 2.0	0.9 ± 2.0	$1.3^{+2.0}_{-1.3}$	67 ± 44
0.328–0.463	4.1 ± 2.1	2.5 ± 2.1	4.8 ± 2.1	16 ± 13
0.463–0.603	1.5 ± 1.8	0.0 ± 1.8	$1.5^{+1.8}_{-1.5}$	0 ± 34
0.603–0.733	3.8 ± 1.7	-0.9 ± 1.7	3.9 ± 1.7	-7 ± 13
0.733–0.813	0.9 ± 2.2	-8.0 ± 2.2	8.0 ± 2.2	-42 ± 8
0.813–0.893	0.6 ± 2.1	-1.2 ± 2.1	$1.4^{+2.1}_{-1.4}$	-32 ± 45
0.893–1.000	-1.5 ± 2.0	0.9 ± 2.0	$1.8^{+2.0}_{-1.8}$	75 ± 33
0.000–1.000	0.7 ± 0.7	-0.5 ± 0.7	0.8 ± 0.7	-19 ± 23

Notes. The uncertainties are given at the 68.3% (1σ) confidence level.

Table 2. Spectral parameters for the best-fit model obtained from the phase-averaged spectro-polarimetric analysis with XSPEC.

Parameter	Value	Unit
N_H	24.6 ± 0.4	10^{22} cm^{-2}
E_{Fe}	6.35 ± 0.01	keV
σ_{Fe}	0.27 ± 0.03	keV
$const_{DU2}$	0.960 ± 0.007	
$const_{DU3}$	0.927 ± 0.007	
Hoton index	0.29 ± 0.05	
PD	0.67 ± 0.64 (<2.3)	%
PA	-36 ± 27	deg
$Flux_{2-8\ keV}$	$8.58^{+0.03}_{-0.08}$	10^{-10} erg cm^{-2} s^{-1}
$Luminosity_{2-8\ keV}$	1.3×10^{36}	erg s^{-1} at $d = 3.5$ kpc
χ^2 (d.o.f.)	1374 (1322)	

Notes. The uncertainties are given at the 68.3% (1σ) confidence level and were obtained using the error command in XSPEC with $\Delta\chi^2 = 1$ for one parameter of interest. The upper limit of the PD (in parentheses) corresponds to the 99% confidence level ($\Delta\chi^2 = 6.635$).

by comparing the pulse profiles in the 4–8 keV energy band for both observations.

3.2. Polarimetric analysis

We analyzed the polarimetric properties of GX 301−2 in the model-independent way by deriving the normalized Stokes parameters $q = Q/I$ and $u = U/I$ and subsequently the PD $= \sqrt{q^2 + u^2}$ and PA $= \frac{1}{2}\arctan(u/q)$ using the pcube algorithm (xpbin tool) in the IXPEOBSSIM package, which follows the description by Kislat et al. (2015) and Baldini et al. (2022). We obtained the phase-averaged values of $q = 0.7 \pm 0.7\%$ and $u = -0.5 \pm 0.7\%$ in the full 2–8 keV energy range (see Fig. 4 for all the DUs separately), implying that no significant polarization in the phase-averaged data is detected. The data were subsequently divided into six energy bins to study a possible energy dependence of the phase-averaged polarization properties for GX 301−2. The measured Stokes parameters are consistent with zero within 2σ.

The polarization properties of XRPs are expected to be strongly variable with pulse phase, and therefore we performed a phase-resolved polarimetric analysis using the pcube algorithm.

Table 3. Spectro-polarimetric parameters in different pulse-phase bins obtained with XSPEC.

Phase	$N_{\rm H}$ (10^{22} cm^{-2})	Photon index	PD (%)	PA (deg)	χ^2/d.o.f.
0.000–0.058	24.4 ± 1.2	0.15 ± 0.14	9.9 ± 3.2	89 ± 9	991/1017
0.058–0.193	23.4 ± 0.7	−0.08 ± 0.08	$1.9^{+1.9}_{-1.9}$ (<6.8)	80 ± 30	1262/1245
0.193–0.328	25.1 ± 0.7	0.11 ± 0.08	$2.0^{+1.9}_{-1.9}$ (<6.8)	66 ± 34	1343/1236
0.328–0.463	24.3 ± 0.7	0.12 ± 0.09	4.9 ± 2.1	15 ± 13	1254/1212
0.463–0.603	26.3 ± 0.6	0.45 ± 0.07	$0.2^{+1.7}_{-0.2}$ (<4.6)	82 ± 90	1321/1269
0.603–0.733	25.6 ± 0.6	0.30 ± 0.06	4.3 ± 1.6	−14 ± 11	1398/1278
0.733–0.813	24.8 ± 0.7	0.24 ± 0.08	7.7 ± 2.0	−46 ± 7	1271/1206
0.813–0.893	26.5 ± 0.7	0.59 ± 0.08	2.8 ± 1.9	−13 ± 22	1273/1212
0.893–1.000	26.8 ± 0.7	0.59 ± 0.08	$1.6^{+1.9}_{-1.6}$ (<6.5)	72 ± 40	1241/1227

Notes. The uncertainties computed using the `error` command are given at the 68.3% (1σ) confidence level ($\Delta\chi^2 = 1$ for one parameter of interest). The upper limits of the PD (in parentheses) correspond to the 99% confidence level ($\Delta\chi^2 = 6.635$) and are quoted when the PD is consistent with zero within 1σ.

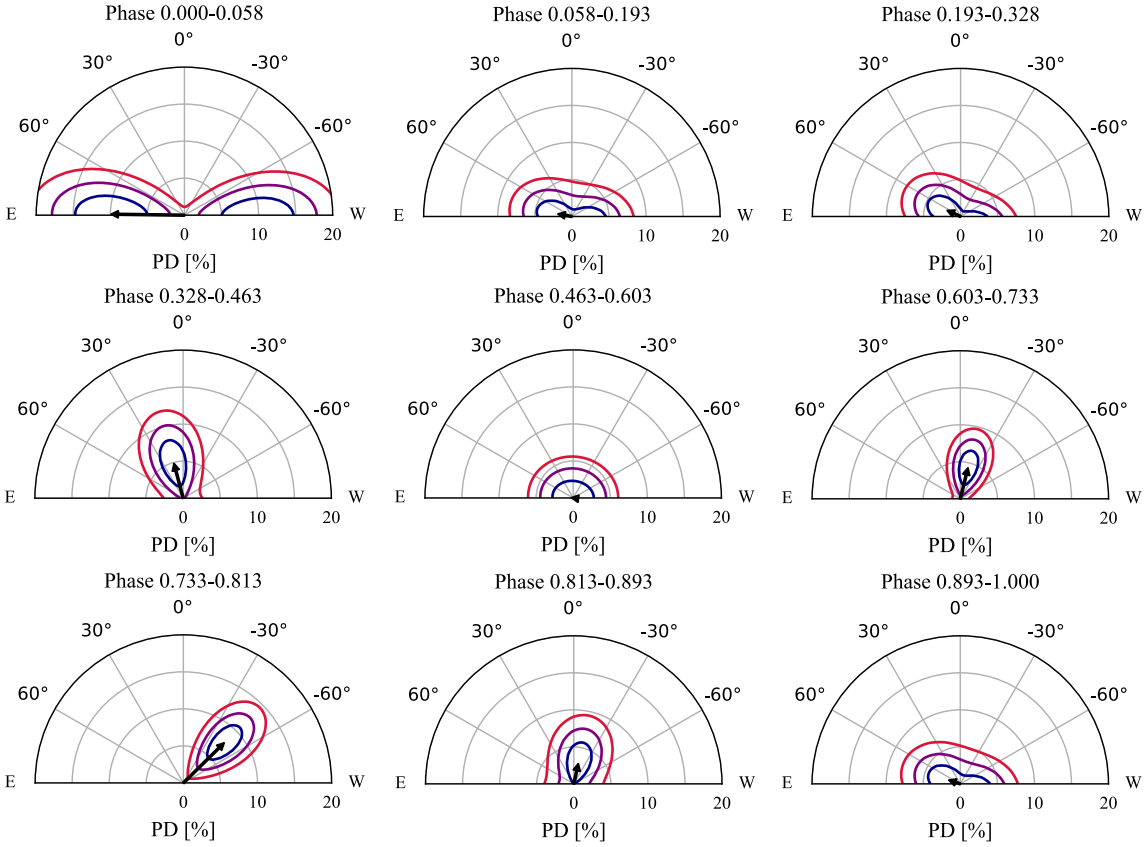

Fig. 7. Polarization vectors of GX 301−2 from the results of the phase-resolved spectro-polarimetric analysis. Contours at 68.3%, 95.45%, and 99.73% confidence levels are shown in blue, purple, and red, respectively.

The data were divided into nine separate phase bins in the full 2–8 keV range. The results are displayed in Fig. 5 and in Fig. 6b,c and are given in Table 1. We found a significant (above 3σ) detection of polarization in two out of the nine phase bins and a marginal detection (above 2σ) in another two bins.

Next, to fully account for the energy dispersion and spectral shape, we performed a model-dependent spectro-polarimetric analysis by simultaneously fitting the Stokes I, Q, and U spectra in XSPEC in order to study the polarization properties as a function of energy. The continuum spectra of XRPs are typically described by purely phenomenological spectral models, such as a power law with a cutoff at high energies. Several models of varying complexity have been used to describe the spectral continuum of GX 301−2. However, for the energy resolution and energy range of IXPE, we used a more simplified model to fit the spectra. This spectral model consists of an absorbed power law (for the absorption we used `tbabs` model with the abundances from Wilms et al. 2000). Additionally, a prominent iron emission line (complex) was also observed, and therefore a Gaussian component was introduced. A re-normalization constant was

used to account for possible discrepancies between the separate DUs (`const`), and for DU1 it was fixed at unity. Finally, the `polconst` polarization model, assuming a constant PD and PA with energy, was applied to the power law, while the Gaussian component was assumed to be unpolarized. The resulting model,

`tbabs` × (`polconst` × `powerlaw+gaussian`) × `const`,

was used to fit both the phase-averaged and the phase-resolved data. A systematic error of 5% was added over the entire 2–8 keV energy range for the phase-averaged spectro-polarimetric analysis. The results of the spectral fitting of the phase-averaged data are given in Table 2. For the phase-averaged data, we did not detect any significant polarization, with a 99% upper limit of PD < 2.3%. The `polconst` polarization model was replaced with the `pollin` (linear energy dependence of the PD and PA) and `polpow` (power-law energy dependence of the PD and PA) models; however, neither one gave an improvement of the fit. Thus, we found no evidence for an energy-dependent polarization.

The same model used for the phase-averaged spectro-polarimetric analysis was used to fit the phase-resolved spectra. However, the cross-calibration constants for DU2 and DU3 were fixed to the best-fit values obtained for the phase-averaged analysis (see Table 2). Due to low statistics in the phase-resolved spectra, the energy and width of the Gaussian component were fixed at the best-fit values from Table 2. The `steppar` command in XSPEC was used to obtain the constraints on polarization parameters. The resulting PD and PA are shown in Figs. 6d,e and given in Table 3. The two different approaches using `pcube` and XSPEC gave compatible results. The 2D contour plots at 68.3%, 95.45%, and 99.73% confidence levels for the PD and PA pair are presented in Fig. 7.

4. Discussion

4.1. Pulsar geometry

The rotating vector model (RVM; Radhakrishnan & Cooke 1969) can be used to constrain the pulsar geometry. Assuming that radiation is dominated by the ordinary mode photons (O-mode), the PA is given by equation (30) in Poutanen (2020):

$$\tan(\mathrm{PA}-\chi_\mathrm{p}) = \frac{-\sin\theta\,\sin(\phi-\phi_0)}{\sin i_\mathrm{p}\cos\theta - \cos i_\mathrm{p}\sin\theta\cos(\phi-\phi_0)}, \quad (1)$$

where χ_p is the position angle (measured from north to east) of the pulsar angular momentum, i_p is the inclination of the pulsar spin to the line of sight, θ is the angle between the magnetic dipole and the spin axis, and ϕ_0 is the phase when the northern magnetic pole passes in front of the observer. If radiation escapes predominantly in the extraordinary mode (X-mode), the position angle of the pulsar angular momentum is $\chi_\mathrm{p} \pm 90°$. In the non-relativistic RVM, the PA does not depend on the PD of the radiation escaping from the NS surface, or any other details. In fact, the polarization plane rotates when radiation travels through the NS magnetosphere up to the adiabatic radius, a few tens of the NS radius (Heyl et al. 2003). At such distances, the dipole field component dominates, and under these circumstances, the RVM model becomes applicable. The general relativistic effects influence the polarization plane only if the NS rotates rapidly (see Poutanen 2020).

In spite of the fact that the observed PAs are not well determined in many phase bins, we can use measurements of the Stokes q and u parameters (which are normally distributed) in all phase bins to get constraints on RVM parameters. For any (q, u) and their error σ_p, the probability density function of the PA, ψ, can be computed as (Naghizadeh-Khouei & Clarke 1993):

$$G(\psi) = \frac{1}{\sqrt{\pi}}\left\{\frac{1}{\sqrt{\pi}} + \eta \mathrm{e}^{\eta^2}\left[1+\mathrm{erf}(\eta)\right]\right\}\mathrm{e}^{-p_0^2/2}. \quad (2)$$

Here, $p_0 = \sqrt{q^2+u^2}/\sigma_\mathrm{p}$ is the "measured" PD in units of the error, $\eta = p_0\cos[2(\psi-\psi_0)]/\sqrt{2}$, $\psi_0 = \frac{1}{2}\arctan(u/q)$ is the central PA obtained from the Stokes parameters, and erf is the error function.

We fit the RVM to the pulse-phase dependence of the (q, u) obtained from `pcube` using the affine invariant Markov chain Monte Carlo (MCMC) ensemble sampler EMCEE package of PYTHON (Foreman-Mackey et al. 2013) and applying the likelihood function $L = \Pi_i G(\psi_i)$ with the product taken over all phase bins. The covariance plot for the RVM parameters is shown in Fig. 8. We note that fitting the PA values obtained from XSPEC with the RVM and assuming Gaussian errors and χ^2 statistics gives nearly identical results.

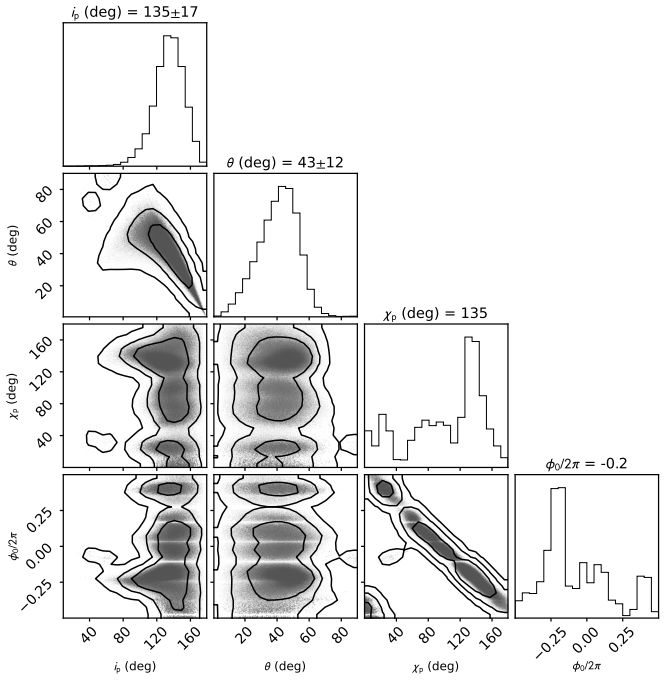

Fig. 8. Corner plot of the posterior distribution for parameters of the RVM model fitted directly to the (q, u) values using the likelihood function (2). The two-dimensional contours correspond to 68.3%, 95.45%, and 99.73% confidence levels. The histograms show the normalized one-dimensional distributions for a given parameter derived from the posterior samples.

It is clear that the inclination and the magnetic obliquity are rather well determined: $i_\mathrm{p} = 135° \pm 17°$ and $\theta = 43° \pm 12°$. However, other parameters allowed for multiple solutions. The reason for this is simple: Most of the detections of polarization are only marginal. The posterior distribution of χ_p has three broad peaks at 25°, 80°, and the strongest one at 135°. These peaks correspond to the peaks in $\phi_0/(2\pi)$ at 0.4, 0.0, and −0.2, respectively.

As a test of our RVM fit to the phase-binned data, we applied an alternative unbinned photon-by-photon analysis (González-Caniulef et al. 2023). We ran MCMC simulations to get the estimates on the RVM parameters. The results are shown in Fig. 9. The photoelectron emission angles for each event were used to constrain an RVM that predicts the distribution of photoelectron angles as a function of the phase. The PA of the best-fit

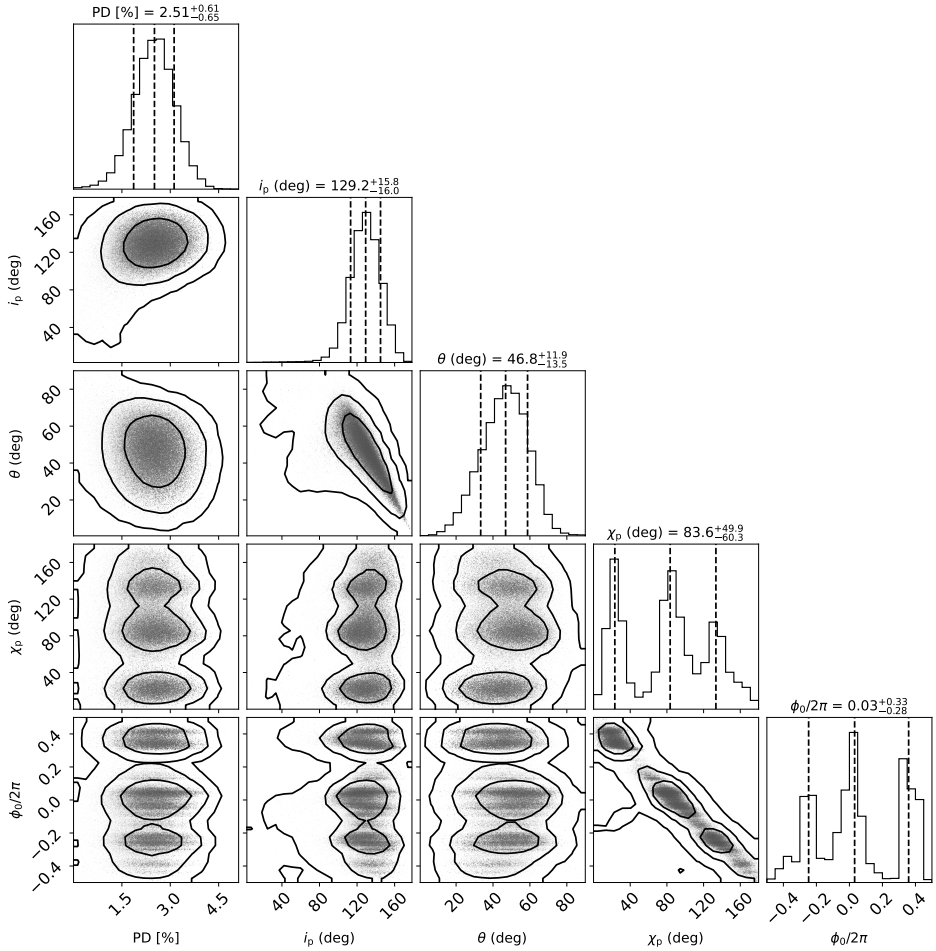

Fig. 9. Same as Fig. 8 but obtained via unbinned analysis (González-Caniulef et al. 2023).

RVM is depicted by an orange curve in Fig. 10. Furthermore, for illustration, we obtained a maximum-likelihood estimate of the PD and PA, assuming constant polarization in each of the fourteen phase bins, as shown by the error bars in the lower two panels of Fig. 10. The mean PD in the frame of the magnetic pole is about 2.5%. The best-fit $i_p = 129° \pm 16°$ and $\theta = 47° \pm 12°$ are in perfect agreement with the RVM fit to the phase-binned data. However, the position angle of the pulsar spin and the zero phase ϕ_0 are not well determined. Here too, the posterior distributions show multiple peaks and strong correlation between these parameters. Three peaks in the distributions of χ_p and ϕ_0 at positions close to those of the phase-binned RVM fits can be seen.

4.2. Scattering by the stellar wind

The relatively low PD detected for GX 301−2 is in line with other XRPs observed with IXPE (Cen X-3, Her X-1, GRO J1008−57, Vela X-1, 4U 1626−67, EXO 2030+375). The low PD is in contradiction with previous theoretical predictions, which estimate PDs as high as 80% (Meszaros et al. 1988; Caiazzo & Heyl 2021). We find it interesting that more luminous XRPs ($L_X \geq 10^{37}$ erg s^{-1}) demonstrate a significantly higher phase-averaged PD, up to 6%–10% in Her X-1 (Doroshenko et al. 2022) and 4%–6% in Cen X-3 (Tsygankov et al. 2022), than the less luminous XRPs. It can be connected with the difference in the physical properties of the radiation regions. In particular, Doroshenko et al. (2022) proposed a model to explain the low PD by means of an overheated upper NS atmosphere with a sharp temperature gradient between the overheated upper atmospheric layer and the underlying cooler layer. The most important component of this model is the point of the so-called vacuum resonance, where the mode conversion occurs. If the point of vacuum resonance is located at the transition between the hot and cool layer, this may result in a low PD. The described model can be correct for relatively low local accretion rates only.

In addition to an intrinsic low polarization, we considered the possibility that the X-ray radiation can be depolarized in the plasma surrounding the XRP because GX 301−2 is significantly more obscured than other XRPs. A detailed qualitative analysis of the reasons for depolarization was presented in Tsygankov et al. (2022). Here, we considered the depolarization of the X-ray flux passing through the surrounding plasma in more detail. The XRP GX 301−2 is subject to the dense stellar wind of its massive companion star. This wind is characterized by a relatively slow velocity and a huge mass-loss rate. Scattering in the wind is expected to reduce intrinsic polarization. Whether or not the wind is able to affect the observed polarization depends on the wind Thomson optical depth, which can be estimated as (Kallman et al. 2015) $\tau_T \simeq 2 \times 10^{-4} \dot{M}_8 a_{12}^{-1} v_{x8}^{-1}$, where $\dot{M}_8$ is the mass-loss rate in units $10^{-8} M_\odot$ yr^{-1}, a_{12} is the separation in units 10^{12} cm, and v_{x8} is the wind velocity at the X-ray source in units 1000 km s^{-1}. For GX 301−2, taking typical values for the wind parameters $\dot{M}_8 \sim 10^3$ and $v_{x8} = 0.3$ as well as the orbital separation at periastron passage $a = a_p \sim 95\,R_\odot$ (i.e., $a_{12} = 6.7$), we obtained the optical depth through the wind of $\tau_T \sim 0.1$.

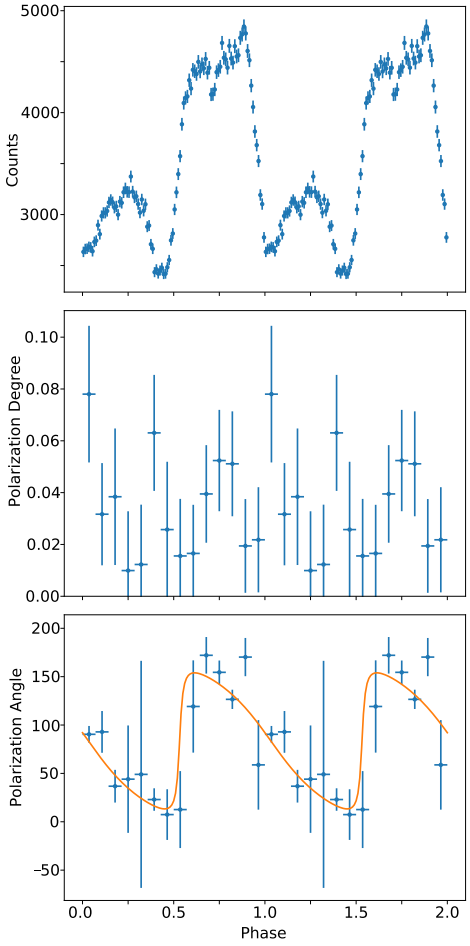

Fig. 10. Pulse profile, PD, and PA obtained from the maximum-likelihood analysis (González-Caniulef et al. 2023). The error bars give the most likely values of PD and PA with $\Delta \ln L = 0.5$ (1σ) confidence regions. The orange curve at the bottom panel shows the best-fit RVM solution with the following parameters $i_p = 129°$, $\theta = 47°$, $\chi_p = 84°$, $\phi_0/(2\pi) = 0.03$.

Our estimate was made under the assumption of a homogeneous, spherically symmetric wind. However, the orbiting NS disturbs the stellar wind, leading to various inhomogeneities in the vicinity of the XRP. As a result, the optical depth along the line of sight can be larger. In the first approximation, this optical depth can be estimated from N_H, assuming that the number of electrons along the line of sight is the same. For the N_H in the range $(5-20)\times10^{23}$ cm^{-2} (Fürst et al. 2018; Nabizadeh et al. 2019; Doroshenko et al. 2010; Ji et al. 2021), we obtained $\tau_T \approx \sigma_T N_H \approx 0.3$–$1.2$.

In this paragraph, we describe our consideration of how the polarized radiation will be depolarized when it is transmitted through the ionized plasma slab. We neglected emission by the plasma itself and assumed that the slab is situated far enough from the X-ray source so that the external flux is directed normally to the slab surface. We then computed the polarization properties of radiation that is transmitted through the slab along its normal. We assumed that the incoming radiation is 100% linearly polarized. We solved the radiation transfer equation accounting for polarization under electron scattering (Chandrasekhar 1960; Sobolev 1963; Suleimanov et al. 2023). We defined the depolarization factor dPD = PD′/PD as the ratio of the PD of the transmitted radiation to that of the incident one. The results of our calculations for different optical depths

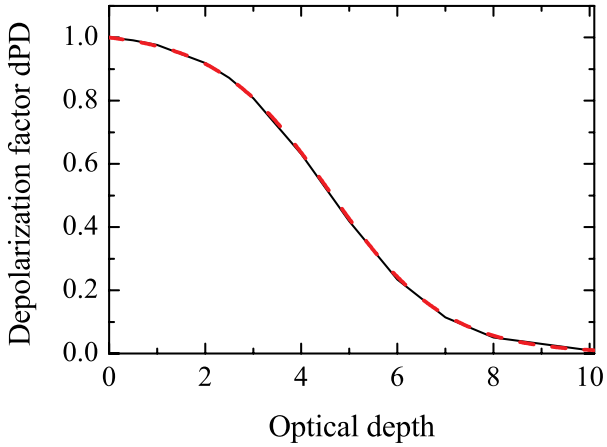

Fig. 11. Dependence of the depolarization factor on the plasma optical depth. The fit with the expression given by Eq. (3) is also shown with the red dashed curve.

of the slab are shown in Fig. 11. It is clear that if the slab is almost transparent ($\tau < 1$), only a small part of the radiation is scattered, and the PD decreases insignificantly. At higher optical depths, the fraction of scattered radiation increases, resulting in a smaller PD, and finally the PD becomes consistent with the case of the pure electron scattering atmosphere (Chandrasekhar 1960; Sobolev 1963) and approaches zero because of the axial symmetry. The dependence of dPD on the slab optical depth τ is well approximated by the expression

$$\mathrm{dPD} = A\left[\exp\left(\frac{\tau-\tau_*}{\Delta\tau}\right)+1\right]^{-1}, \quad (3)$$

where $\tau_* = 4.6$ is the optical depth providing dPD = 0.5, $\Delta\tau = 1.2$ is a smearing parameter, and $A = \exp(-\tau_*/\Delta\tau)+1 \approx 1.02$ is a normalization constant. We note that τ is the total optical depth including not only electron scattering but also the free-free and bound-free absorption. Figure 11 shows that, in principle, the PD can decrease by a factor of two for $\tau \sim 5$, but such a large optical depth of the envelope around the XRP is clearly too large and would lead to a dramatic decrease of the pulsed fraction, which is not observed. Thus, we can conclude that scattering in the wind is not a likely source of a relatively low PD.

In addition to scattering, the wind may also reprocess some radiation of the XRP. In particular, the strength of fluorescent iron lines Kα and Kβ observed from GX 301−2 (see, e.g., Ji et al. 2021) correlates with the X-ray flux and with the local absorption. The lines contribute about 10% of the flux in the IXPE band. Thus, these unpolarized lines can produce a depolarization factor of about 0.9, which means that they cannot significantly depolarize the XRP radiation.

5. Summary

The XRP GX 301−2 was observed by IXPE between 2022 July 29 and August 3 during a pre-periastron flare. Simultaneous observations of GX 301−2 were carried out by the ART-XC telescope between 2022 July 30 and August 1. The main results of our study of the polarimetric properties of GX 301−2 are summarized as follows:

1. We have not detected a significant polarization in the phase-averaged data with an upper limit to the PD of 2.3% (at 99% confidence level) in the full 2–8 keV energy range of IXPE. Likewise, no significant polarization was detected in any energy bin in the phase-averaged data.

2. The phase-resolved polarimetric analysis revealed a significant detection of polarization in two out of nine phase bins and a marginal detection in three bins, with the PD ranging from ∼3% to ∼10% and the PA varying in a very wide range from ∼0° to ∼160°.
3. Application of the RVM to the phase-resolved PA (accounting even for the points with low significance) allowed us to estimate the inclination of the NS rotation axis to the line of sight of $i_p \approx 130°-140°$ and the magnetic obliquity of $\theta \approx 40°-50°$. The measured pulsar spin inclination is in good agreement with the orbital inclination of 52°–78°, with some preference toward lower values determined by Leahy & Kostka (2008). We note that the preferred lowest orbital inclination is equivalent to 128°. Thus, it is possible that the rotation axis of the pulsar is nearly aligned with the orbital axis. On the other hand, the NS in the system might rotate retrogradely, as was proposed by Mönkkönen et al. (2020). The position angle of the pulsar spin and the zero phase, when the northern magnetic pole passes in front of the observer, allow for multiple solutions. We find excellent agreement between phase-binned and unbinned analyses.
4. The contribution of the reprocessed radiation and scattering in the surrounding matter can depolarize the intrinsic XRP flux by no more than 10%–15%.

Additional observations of GX 301−2 with IXPE may improve the statistics, allowing us to get better constraints on the pulsar axis position angle and the zero phase ϕ_0.

Acknowledgements. The Imaging X-ray Polarimetry Explorer is a joint US and Italian mission. The US contribution is supported by the National Aeronautics and Space Administration (NASA) and led and managed by its Marshall Space Flight Center (MSFC), with industry partner Ball Aerospace (contract NNM15AA18C). The Italian contribution is supported by the Italian Space Agency (Agenzia Spaziale Italiana, ASI) through contract ASI-OHBI-2017-12-I.0, agreements ASI-INAF-2017-12-H0 and ASI-INFN-2017.13-H0, and its Space Science Data Center (SSDC) with agreements ASI-INAF-2022-14-HH.0 and ASI-INFN 2021-43-HH.0, and by the Istituto Nazionale di Astrofisica (INAF) and the Istituto Nazionale di Fisica Nucleare (INFN) in Italy. This research used data products provided by the IXPE Team (MSFC, SSDC, INAF, and INFN) and distributed with additional software tools by the High-Energy Astrophysics Science Archive Research Center (HEASARC), at NASA Goddard Space Flight Center (GSFC). This research has been supported by Deutsche Forschungsgemeinschaft (DFG) grant WE 1312/59-1 (VFS). We also acknowledge support from the German Academic Exchange Service (DAAD) travel grant 57525212 (VFS, VD), the Academy of Finland grants 333112, 349144, 349373, and 349906 (SST, JP), the Väisälä Foundation (SST), CNES fellowship grant (DG-C), Natural Sciences and Engineering Research Council of Canada (JH), the Russian Science Foundation grant 19-12-00423 (AAL, SVM, AES), and UKRI Stephen Hawking fellowship (AAM).

References

Abarr, Q., Baring, M., Beheshtipour, B., et al. 2020, ApJ, 891, 70
Arnaud, K. A. 1996, in Astronomical Data Analysis Software and Systems V, eds. G. H. Jacoby, & J. Barnes (San Francisco: Astron. Soc. Pac.), ASP Conf. Ser., 101, 17
Bailer-Jones, C. A. L., Rybizki, J., Fouesneau, M., Mantelet, G., & Andrae, R. 2018, AJ, 156, 58
Baldini, L., Barbanera, M., Bellazzini, R., et al. 2021, Astropart. Phys., 133, 102628
Baldini, L., Bucciantini, N., Lalla, N. D., et al. 2022, SoftwareX, 19, 101194
Basko, M. M., & Sunyaev, R. A. 1976, MNRAS, 175, 395
Becker, P. A., Klochkov, D., Schönherr, G., et al. 2012, A&A, 544, A123
Caiazzo, I., & Heyl, J. 2021, MNRAS, 501, 109
Chandrasekhar, S. 1960, Radiative Transfer (New York: Dover)
Di Marco, A., Soffitta, P., Costa, E., et al. 2023, AJ, 165, 143
Doroshenko, V., Santangelo, A., Suleimanov, V., et al. 2010, A&A, 677, A57
Doroshenko, V., Poutanen, J., Tsygankov, S. S., et al. 2022, Nat. Astron., 6, 1433
Doroshenko, V., Poutanen, J., Heyl, J., et al. 2023, A&A, 677, A57
Foreman-Mackey, D., Hogg, D. W., Lang, D., & Goodman, J. 2013, PASP, 125, 306
Forsblom, S. V., Poutanen, J., Tsygankov, S. S., et al. 2023, ApJ, 947, L20
Fürst, F., Falkner, S., Marcu-Cheatham, D., et al. 2018, A&A, 620, A153
Gehrels, N., Chincarini, G., Giommi, P., et al. 2004, ApJ, 611, 1005
González-Caniulef, D., Caiazzo, I., & Heyl, J. 2023, MNRAS, 519, 5902
Hammerschlag-Hensberge, G., Zuiderwijk, E. J., van den Heuvel, E. P. J., & Hensberge, H. 1976, A&A, 49, 321
Harding, A. K., & Lai, D. 2006, Rep. Prog. Phys., 69, 2631
Heyl, J. S., Shaviv, N. J., & Lloyd, D. 2003, MNRAS, 342, 134
Ji, L., Doroshenko, V., Suleimanov, V., et al. 2021, MNRAS, 501, 2522
Kallman, T., Dorodnitsyn, A., & Blondin, J. 2015, ApJ, 815, 53
Kaper, L., van der Meer, A., & Najarro, F. 2006, A&A, 457, 595
Kislat, F., Clark, B., Beilicke, M., & Krawczynski, H. 2015, Astropart. Phys., 68, 45
Koh, D. T., Bildsten, L., Chakrabarty, D., et al. 1997, ApJ, 479, 933
Leahy, D. A., & Kostka, M. 2008, MNRAS, 384, 747
Malacaria, C., Heyl, J., Doroshenko, V., et al. 2023, A&A, 675, A29
Marshall, H. L., Ng, M., Rogantini, D., et al. 2022, ApJ, 940, 70
Meszaros, P., Novick, R., Szentgyorgyi, A., Chanan, G. A., & Weisskopf, M. C. 1988, ApJ, 324, 1056
Mönkkönen, J., Doroshenko, V., Tsygankov, S. S., et al. 2020, MNRAS, 494, 2178
Mushtukov, A., & Tsygankov, S. 2022, in Handbook of X-ray and Gamma-ray Astrophysics, eds. C. Bambi, & A. Santangelo (Singapore: Springer)
Mushtukov, A. A., Suleimanov, V. F., Tsygankov, S. S., & Poutanen, J. 2015, MNRAS, 447, 1847
Mushtukov, A. A., Tsygankov, S. S., Poutanen, J., et al. 2023, MNRAS, 524, 2004
Nabizadeh, A., Mönkkönen, J., Tsygankov, S. S., et al. 2019, A&A, 629, A101
Naghizadeh-Khouei, J., & Clarke, D. 1993, A&A, 274, 968
Pavlinsky, M., Tkachenko, A., Levin, V., et al. 2021, A&A, 650, A42
Poutanen, J. 2020, A&A, 641, A166
Pravdo, S. H., Day, C. S. R., Angelini, L., et al. 1995, ApJ, 454, 872
Radhakrishnan, V., & Cooke, D. J. 1969, App. Lett., 3, 225
Sobolev, V. V. 1963, A Treatise on Radiative Transfer (Princeton: Van Nostrand)
Soffitta, P., Baldini, L., Bellazzini, R., et al. 2021, AJ, 162, 208
Suleimanov, V. F., Poutanen, J., Doroshenko, V., & Werner, K. 2023, A&A, 673, A15
Sunyaev, R., Arefiev, V., Babyshkin, V., et al. 2021, A&A, 656, A132
Treuz, S., Doroshenko, V., Santangelo, A., & Staubert, R. 2018, ArXiv e-prints [arXiv:1806.11397]
Tsygankov, S. S., Doroshenko, V., Poutanen, J., et al. 2022, ApJ, 941, L14
Tsygankov, S. S., Doroshenko, V., Mushtukov, A. A., et al. 2023, A&A, 675, A48
Weisskopf, M. C., Soffitta, P., Baldini, L., et al. 2022, JATIS, 8, 026002
White, N. E., Mason, K. O., Huckle, H. E., Charles, P. A., & Sanford, P. W. 1976, ApJ, 209, L119
Wilms, J., Allen, A., & McCray, R. 2000, ApJ, 542, 914

[1] Institut für Astronomie und Astrophysik, Universität Tübingen, Sand 1, 72076 Tübingen, Germany
e-mail: suleimanov@astro.uni-tuebingen.de
[2] Department of Physics and Astronomy, 20014 University of Turku, Finland
[3] INAF Istituto di Astrofisica e Planetologia Spaziali, Via del Fosso del Cavaliere 100, 00133 Roma, Italy
[4] Institut de Recherche en Astrophysique et Planétologie, UPS-OMP, CNRS, CNES, 9 avenue du Colonel Roche, BP 44346, 31028 Toulouse Cedex 4, France
[5] University of British Columbia, Vancouver, BC V6T 1Z4, Canada
[6] Space Research Institute (IKI) of Russian Academy of Sciences, Prosoyuznaya ul 84/32, 117997 Moscow, Russian Federation
[7] International Space Science Institute, Hallerstrasse 6, 3012 Bern, Switzerland
[8] Astrophysics, Department of Physics, University of Oxford, Denys Wilkinson Building, Keble Road, Oxford OX1 3RH, UK
[9] National Research University Higher School of Economics, Faculty of Physics, 101000 Myasnitskaya ul. 20, Moscow, Russia
[10] Instituto de Astrofísicade Andalucía – CSIC, Glorieta de la Astronomía s/n, 18008 Granada, Spain
[11] INAF Osservatorio Astronomico di Roma, Via Frascati 33, 00040 Monte Porzio Catone (RM), Italy

[12] Space Science Data Center, Agenzia Spaziale Italiana, Via del Politecnico snc, 00133 Roma, Italy
[13] INAF Osservatorio Astronomico di Cagliari, Via della Scienza 5, 09047 Selargius (CA), Italy
[14] Istituto Nazionale di Fisica Nucleare, Sezione di Pisa, Largo B. Pontecorvo 3, 56127 Pisa, Italy
[15] Dipartimento di Fisica, Università di Pisa, Largo B. Pontecorvo 3, 56127 Pisa, Italy
[16] NASA Marshall Space Flight Center, Huntsville, AL 35812, USA
[17] Dipartimento di Matematica e Fisica, Università degli Studi Roma Tre, via della Vasca Navale 84, 00146 Roma, Italy
[18] Istituto Nazionale di Fisica Nucleare, Sezione di Torino, Via Pietro Giuria 1, 10125 Torino, Italy
[19] Dipartimento di Fisica, Università degli Studi di Torino, Via Pietro Giuria 1, 10125 Torino, Italy
[20] INAF Osservatorio Astrofisico di Arcetri, Largo Enrico Fermi 5, 50125 Firenze, Italy
[21] Dipartimento di Fisica e Astronomia, Università degli Studi di Firenze, Via Sansone 1, 50019 Sesto Fiorentino (FI), Italy
[22] Istituto Nazionale di Fisica Nucleare, Sezione di Firenze, Via Sansone 1, 50019 Sesto Fiorentino (FI), Italy
[23] Agenzia Spaziale Italiana, Via del Politecnico snc, 00133 Roma, Italy
[24] Science and Technology Institute, Universities Space Research Association, Huntsville, AL 35805, USA
[25] Istituto Nazionale di Fisica Nucleare, Sezione di Roma "Tor Vergata", Via della Ricerca Scientifica 1, 00133 Roma, Italy
[26] Department of Physics and Kavli Institute for Particle Astrophysics and Cosmology, Stanford University, Stanford, California 94305, USA
[27] Université Grenoble Alpes, CNRS, IPAG, 38000 Grenoble, France
[28] Astronomical Institute of the Czech Academy of Sciences, Bočnń II 1401/1, 14100 Praha 4, Czech Republic
[29] RIKEN Cluster for Pioneering Research, 2-1 Hirosawa, Wako, Saitama 351-0198, Japan
[30] Cahill Center for Astronomy and Astrophysics, California Institute of Technology, Pasadena, CA 91125, USA
[31] Yamagata University, 1-4-12 Kojirakawa-machi, Yamagata-shi 990-8560, Japan
[32] Osaka University, 1-1 Yamadaoka, Suita, Osaka 565-0871, Japan
[33] International Center for Hadron Astrophysics, Chiba University, Chiba 263-8522, Japan
[34] Institute for Astrophysical Research, Boston University, 725 Commonwealth Avenue, Boston, MA 02215, USA
[35] Department of Astrophysics, St. Petersburg State University, Universitetsky pr. 28, Petrodvoretz, 198504 St. Petersburg, Russia
[36] Department of Physics and Astronomy and Space Science Center, University of New Hampshire, Durham, NH 03824, USA
[37] Physics Department and McDonnell Center for the Space Sciences, Washington University in St. Louis, St. Louis, MO 63130, USA
[38] Finnish Centre for Astronomy with ESO, 20014 University of Turku, Finland
[39] Istituto Nazionale di Fisica Nucleare, Sezione di Napoli, Strada Comunale Cinthia, 80126 Napoli, Italy
[40] Université de Strasbourg, CNRS, Observatoire Astronomique de Strasbourg, UMR 7550, 67000 Strasbourg, France
[41] MIT Kavli Institute for Astrophysics and Space Research, Massachusetts Institute of Technology, 77 Massachusetts Avenue, Cambridge, MA 02139, USA
[42] Graduate School of Science, Division of Particle and Astrophysical Science, Nagoya University, Furo-cho, Chikusa-ku, Nagoya, Aichi 464-8602, Japan
[43] Hiroshima Astrophysical Science Center, Hiroshima University, 1-3-1 Kagamiyama, Higashi-Hiroshima, Hiroshima 739-8526, Japan
[44] University of Maryland, Baltimore County, Baltimore, MD 21250, USA
[45] NASA Goddard Space Flight Center, Greenbelt, MD 20771, USA
[46] Center for Research and Exploration in Space Science and Technology, NASA/GSFC, Greenbelt, MD 20771, USA
[47] Department of Physics, University of Hong Kong, Pokfulam, Hong Kong
[48] Department of Astronomy and Astrophysics, Pennsylvania State University, University Park, PA 16801, USA
[49] Center for Astrophysics, Harvard & Smithsonian, 60 Garden St, Cambridge, MA 02138, USA
[50] INAF Osservatorio Astronomico di Brera, via E. Bianchi 46, 23807 Merate (LC), Italy
[51] Dipartimento di Fisica e Astronomia, Università degli Studi di Padova, Via Marzolo 8, 35131 Padova, Italy
[52] Dipartimento di Fisica, Università degli Studi di Roma "Tor Vergata", Via della Ricerca Scientifica 1, 00133 Roma, Italy
[53] Department of Astronomy, University of Maryland, College Park, Maryland 20742, USA
[54] Mullard Space Science Laboratory, University College London, Holmbury St Mary, Dorking, Surrey RH5 6NT, UK
[55] Anton Pannekoek Institute for Astronomy & GRAPPA, University of Amsterdam, Science Park 904, 1098, XH Amsterdam, The Netherlands
[56] Guangxi Key Laboratory for Relativistic Astrophysics, School of Physical Science and Technology, Guangxi University, Nanning 530004, PR China